2022 9th IEEE RAS/EMBS International Conference for Biomedical Robotics and Biomechatronics (BioRob) | 978-1-6654-5849-8/22/$31.00 ©2022 IEEE | DOI: 10.1109/BIOROB52689.2022.9925327

Using Dynamic Simulations to Estimate the Feasible Stability Region of Feet-In-Place Balance Recovery for Lower-Limb Exoskeleton Users

Keaton A. Inkol and John McPhee

***Abstract*— In recent years, research into the balancing capabilities of lower-limb exoskeletons has increased with hopes of achieving "crutch-less" stance and ambulation. However, achieving upright stability in underactuated bipedal robotics is difficult. Disturbances due to end-user interactions and actuator limitations further complicate any solutions. The current study was therefore aimed at establishing the generalized balancing capabilities of active robotic lower-limb exoskeletons through the use of predictive dynamic simulations. The ability to balance was assessed through the use of the feasible stability region (FSR), which is the region in whole-body center of mass (COM) position-velocity space where it is possible to recover upright balance through termination of the COM velocity. Direct collocation optimal control was used to estimate the baseline FSR for the human-only and human-exoskeleton system under various conditions. Additionally, Pareto optimization was used to establish trade-offs between the FSR and the motor torques that generate the necessary balance strategies, which determine the FSR. In general, our results indicated that baseline human-only and human-exoskeleton systems share similar balancing capabilities in terms of the FSR, regardless of the device's end-user mobility; however, features of the exoskeleton like high joint-level impedance and a shifted center of mass have detrimental impacts to the overall FSR size. Results from the Pareto optimization suggest that the full FSR can be nearly reached with a fraction of the required motor torques, thus protecting both the device and user. Future work will expand the current analyses to stepping strategies and control-design implementation in the Technaid Exo-H3.**

I. INTRODUCTION

For many individuals living with impaired mobility, active and passive lower-limb exoskeletons offer a potentially life-changing improvement in the ability to stand, ambulate, and complete tasks of daily living. While the state-of-the-art is promising, there remain many caveats that prevent potential end-users from integrating these devices into their livelihood. One notable issue is in the balancing capabilities of these devices [1–5]. Typically, the designers of these devices require the end-user to use an additional device to prevent falls, e.g., crutches. Evidently, this solution reduces functionality by removing free use of the arms during device operation, thus impacting the user's decision to use an exoskeleton.

Recent research has taken the initiative to investigate the issue of balancing while wearing robotic exoskeletons. Control of standing balance often relies on some variation of model-based [1], [5] or joint-level control [2], [6] that considers the spectrum of human balance strategies reported in the literature [7], e.g. the ankle and hip strategy. Additionally, authors like Gurriet et al. [3] have proposed model-based control schemes rooted in zero dynamics that are capable of providing stable locomotor patterns in paraplegics. Often, especially in the context of rehabilitation, control designers must consider whether the device behaves fully autonomously or provides human-in-charge assistance, which requires consideration of human-exoskeleton interactions and intent detection within the balance control schemes [2], [8].

An established method of analyzing the balancing capabilities of a biped in balance recovery is the feasible stability region (FSR) [10], [11]. For balance in the sagittal plane, the concept states that so long as the *horizontal* position and velocity of the whole-body center of mass (COM) are within the "stable" region of phase-space, the biped will not fall. These boundaries are intrinsically dependent on the system dynamics and are closely related to concepts like capturability [12] and foot placement estimation [13]. When wearing a lower-limb exoskeleton, the COM is typically lowered (depending on the device), which in theory increases the magnitude of COM velocity that can be recovered from [14]. However, the device's torque generating capabilities, joint-level impedance, and dead times resulting from characteristics of the actuators, sensors, etc. may have the opposite effect. Likewise, constraining or minimizing torque or power generation in the device's actuators to prevent damage may also affect the device's ability to terminate a forward fall. In dynamic biomechanical simulations, minimizing human muscle activations has been suggested to promote balance recovery strategies that avoid energetically costly trunk rotations [26]; however, it is not clear how restricting motor inputs may limit the FSR in biomechatronic devices.

The goal of the current study was to use "what-if" dynamic simulations and optimal control to investigate how lower-limb robotic exoskeleton dynamics impact the FSR of the human end-user. Specifically, we investigated how the FSR of the integrated system, wherein the human has generalized muscle weakness (i.e. mimicking a high level of spinal lesions) and the device must replace active muscle torques, compares to that of a user with full mobility. Additionally, we used our computational models to assess the trade-off between FSR boundary and motor torque generation in the device via Pareto optimization.

II. MODELING OF SYSTEM DYNAMICS

A. Human Biomechanics

A floating-base sagittal plane model of human upright stance was created in MapleSim 2021 (Maplesoft, Canada).

This work was funded by the Canada Research Chairs Program (J.M) and the University of Waterloo (K.A.I)

Keaton A. Inkol and John McPhee are with the Department of Systems Design Engineering, University of Waterloo, 200 University Ave W, Canada kainkol@uwaterloo.ca

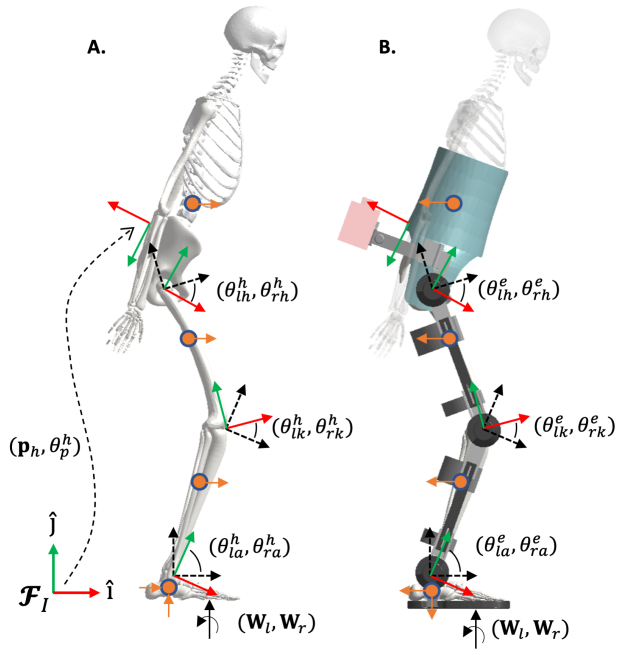

Fig. 1. Schematic of the floating-base human-only (A) and lower-limb exoskeleton dynamic models (B, based on the Technaid Exo-H3), with each systems' nine degrees of freedom highlighted. Note that the human is shown transparently in B to highlight how the exoskeleton fits the user.

It was assumed that the human was a 20-30 year old male with the following characteristics: height = 1.80 m, mass = 75 kg. The model consisted of 16 rigid bodies based on the anthropometric definitions provided in de Leva [15]. Adopting the convention in [3], the model consisted of nine coordinates, $\mathbf{q}_h = [\mathbf{p}_h, \theta^h_p, \phi_h]^T \in \mathbb{R}^9$ (see Fig 1). Revolute joints were used at the left and right ankle, knee and hip ($\phi_h \in \mathbb{R}^6$) in addition to a planar joint connecting the body-fixed pelvis frame to the inertial frame ($\mathbf{p}_h, \theta^h_p$). It was assumed that the pelvis, trunk, head and arms were rigidly locked together. The bipedal dynamics can be thus expressed as a system of differential algebraic equations (DAEs),

$$\mathbf{M}_h(\mathbf{q}_h)\ddot{\mathbf{q}}_h = \boldsymbol{\Gamma}(\mathbf{q}_h, \dot{\mathbf{q}}_h, \boldsymbol{\tau}_{\text{mtg}}) + \{\boldsymbol{\Phi}(\mathbf{q}_h)\}^T_q \boldsymbol{\lambda} \quad (1)$$

$$\boldsymbol{\Phi} = \mathbf{0} \quad (2)$$

where $\mathbf{M}_h \in \mathbb{R}^{9\times 9}$ is the mass matrix, $\boldsymbol{\Phi} \in \mathbb{R}^{m\times 1}$ is a set of m algebraic constraints, and $\boldsymbol{\Gamma} \in \mathbb{R}^{9\times 1}$ is a vector containing torques resulting from gravity and Coriolis/centrifugal effects in addition to those generated by musculature. For a floating-base biped model with both feet-in-place, $\boldsymbol{\Phi}$ consists of 6 equations describing the static base of support. In the current paper, we assume that the right and left foot share the same position in the sagittal plane. The Jacobian $\{\boldsymbol{\Phi}\}_q$, then maps the Lagrange multipliers $\boldsymbol{\lambda}$ (right/left foot-ground contact wrenches) to constraint torques/forces as dictated by each element of $\mathbf{q}_h$, reducing the degrees of freedom to 3.

Biofidelic muscle torques $\boldsymbol{\tau}_{\text{mtg}}$ were generated using muscle torque generators (MTGs), which are rotational single muscle equivalents that negate the need to define complex musculoskeletal geometry [16], [17]. The resulting torques were evaluated as

$$(\boldsymbol{\tau}_{\text{mtg}})_i = \tau_{\text{mtg}}(u_i, \mathbf{q}, \dot{\mathbf{q}}) = u_i \tau_{\max} \mathrm{t}^{\mathrm{A}}(\mathbf{q}) \mathrm{t}^{\mathrm{V}}(\dot{\mathbf{q}}) + \mathrm{t}^{\mathrm{P}}(\mathbf{q}, \dot{\mathbf{q}}) \quad (3)$$

where each MTG is activated by signal $u_i(t) \in [0,1]$, which ignores excitation-contraction dynamics.

A total of 12 muscle torque generators were used to drive the human: one flexor and extensor per element of ϕ_h. The constitutive equations and parameters of the angle and angular velocity-scaling functions t^{A} and t^{V} were based on the model and data presented in [19] and subsequently fit to a spline of 5th-order Bezier curves [17]. Doing so avoided issues associated with the equations in [19], e.g., when t^{A} or $\mathrm{t}^{\mathrm{V}} < 0$, and yielded C^2-continuous curves with respect to $\mathbf{q}$ and $\dot{\mathbf{q}}$, which are well-suited for use in gradient-based optimization procedures.

Passive torques arising from viscoelastic components in parallel to the joint ($\mathrm{t}^{\mathrm{P}} = \mathrm{t}^{\mathrm{S}} + \mathrm{t}^{\mathrm{D}}$) were based on a combination of sources. The exponential stiffness model by Riener and Edrich [20], used in previous assistive device simulations [1], was implemented herein to capture end-range-of-motion stiffness and the effects of biarticular musculature in t^{S}. Joint-level damping t^{D}, important for suppressing high-frequencies in the underlying dynamics, was implemented as,

$$\mathrm{t}^{\mathrm{D}} = -c\dot{\theta}(1 + g(\theta; -1, \theta_{ub}) + g(\theta; 1, \theta_{lb})) \quad (4)$$

where

$$g(\theta; s, \theta_b, \cdot) = e^{-ks(\theta - \theta_b)} \quad (5)$$

and θ_{ub} and θ_{lb} indicate the joint angles at which $g = 1$ [17]. Additionally, c was set to 0.1 Nms/rad as suggested by Yamaguchi [18]. Unlike [17], the structure of (4) permits damping across all velocities, instead of only towards the end range of motion, while still suppressing vibrations at end-ranges of motion where the stiffness increases exponentially.

B. Assistive Device Model

The dynamics of the lower-limb assistive device model shared the same floating-base formulation as the human model, with generalized coordinates $\mathbf{q}_e = [\mathbf{p}_e, \theta^p_e, \phi_e]^T \in \mathbb{R}^9$ where $(\mathbf{p}_e, \theta^p_e)$ are the planar coordinates of trunk/pelvis orthosis and ϕ_e contains lower-limb joint angles. The inertial characteristics of the device were based on previous measurements of rigid body inertia in the Technaid Exo-H3 robotic exoskeleton [1]. Setting the generalized coordinates such that $\mathbf{q}_h = \mathbf{q}_e$ (i.e., human and device joint axes are aligned at all times, [3]), we can merge the human and exoskeleton dynamics (human-exo) resulting in equations of the same dimension as (1) and avoiding the need to solve for interaction forces, i.e. for the integrated human-exo coordinates $\mathbf{q}_{he}$, $\dim(\mathbf{q}_{he}) = \dim(\mathbf{q}_h)$.

For the current simulation experiment, device actuators were assumed to be a combination of DC motor with strain-wave gearing. Harmonic drives are often used in assistive devices due to their combination of small size and high gear ratio. Moment of inertia of the rotor and gearing's wave generator were amplified by the squared gear ratio and included in the mass matrix. As the activation dynamics were

TABLE I
MODELED ACTUATOR PARAMETERS

Description	Value
*DC Motor**	
Nominal Voltage	48 V
Resistance (R)	1.03 Ω
Torque Constant (K)	0.0448 Nms/rad
Motor Mass	0.72 kg
Rotor Moment of Inertia	1.01×10^{-5} kg m^2
Gearing†	
Gear Ratio (N)	50
Moment of Inertia	2.60×10^{-4} kg m^2
Breakway Friction (τ_{brk})	9.42 Nm
Coulomb Friction (τ_{c})	7.97 Nm
Viscous Friction (μ_o)	4.93 Nms/rad
Transition Velocity (ω_t)	0.025 rad/s

*Based on Maxon EC-max 40 BLDC motor [23]
†Based on Harmonic Drive FR-32-50-2-GR [24]

ignored in the human's MTGs, the relatively low inductance in the motor was also ignored. Thus, the motor torque for a given joint could be expressed algebraically from the DC motor equations as simply,

$$\tau_m = \frac{K}{R}(V - K\dot{\theta}_m), \quad \dot{\theta}_m = -N\dot{\theta}_o \tag{6}$$

where R and K are the motor's resistance and torque constant respectively, $\dot{\theta}_o$ is the speed of the output shaft and N is the drive's gear ratio. Given the use of strain-wave gearing, joint-level impedance resulting from friction between the flexspine (free) and circular spine (fixed) should be considered [21]. Adopting the Brown and McPhee [22] velocity-dependent friction model, the final actuator force can be expressed as

$$\tau_o = -(\tau_{\text{brk}} - \tau_{\text{c}})\frac{\frac{\dot{\theta}_o}{\omega_t}}{\frac{1}{4}\left(\frac{\dot{\theta}_o}{\omega_t}\right)^2 + \frac{3}{4}} - \tau_{\text{c}}\tanh\left(4\frac{\dot{\theta}_o}{\omega_t}\right) - \mu_o\dot{\theta}_o - N\tau_m \tag{7}$$

where τ_{brk} and τ_{c} represent the breakaway and Coulomb torques arising from dry friction, while μ_o is the coefficient of viscous friction. Here, the benefit of this model is its simple implementation, continuity, and ability to mimic stiction.

Table I contains the actuator parameters used in simulations. The motor selected was capable of outputting 2.08 Nm in the stall condition [23]. The harmonic drive selected had a gear ratio of 50:1 [24], which permitted momentary torques up to 216 Nm. Gearing friction parameters were adopted from an analysis of a harmonic drive with equivalent speed reduction [21]. The resulting actuator was thus capable of generating torques up to 104 Nm when stalled, which is comparable to the maximal isometric torque generated by the human plantarflexors [19].

III. FEASIBLE STABILITY REGION

w

A. Optimal Control Problem Formulation

The FSR for the human-only and human-exo models balancing with feet-in-place were determined through direct collocation optimal control. Direct collocation involves parameterization of the continuous state ($\mathbf{X} = [\mathbf{x}_1, \mathbf{x}_2, ..., \mathbf{x}_n]^T$) and control trajectories ($\mathbf{U} = [\mathbf{u}_1, \mathbf{u}_2, ..., \mathbf{u}_n]^T$) into discrete arrays consisting of n nodes or knot points that span the entire prediction horizon $[t_0, t_f]$. States consist of the concatenation of generalized coordinates with velocities. Note the notation $\mathbf{x}_i = \mathbf{x}(t_0 + (i-1)\delta t)$ where $\delta t = (t_f - t_0)(n-1)^{-1}$.

In general, the continuous formulation of the optimal control problem that solves for the FSR was,

$$\arg\min_{\mathbf{X},\mathbf{U}} \{-\dot{\mathbf{r}}_{\text{cm}}(t_0)\cdot\hat{\mathbf{i}}\} \tag{8}$$

subject to

$$\mathbf{r}_{\text{cm}}(t_0)\cdot\hat{\mathbf{i}} = r_0 \tag{9}$$

$$\dot{\mathbf{x}} = \mathbf{F}(\mathbf{x}(t), \mathbf{u}(t), t) \tag{10}$$

$$\mathbf{h}(\mathbf{x}(t), \mathbf{u}(t)) \leq 0 \tag{11}$$

$$\mathbf{g}(\mathbf{x}(t), \mathbf{u}(t)) = 0 \tag{12}$$

which herein searches for the maximum initial COM velocity $\dot{\mathbf{r}}_{\text{cm}}$ in the forward direction $\hat{\mathbf{i}}$ that can be terminated given a set initial horizontal COM position r_0. By solving this problem for the set of COM positions normalized to foot length $\{0, 0.25, ..., 1.00\}$ (0 = toe, 1 = heel), we could establish the system's FSR for when the COM is within the base of support. The prediction horizon was set to 1.5 seconds [26] and contained 60 nodes. Equation (10), i.e., (1) and (2) converted to a system of ordinary differential equations, was enforced numerically through Hermite-Simpson collocation. Inequality and equality constraints (11-12) were enforced to prevent the zero moment point (ZMP) from existing outside of the physical base of support boundaries, slipping of the feet (assuming a static coefficient of friction of 0.80 [10]), and the vertical ground-reaction forces from "pulling" on the feet. At t_f, the horizontal COM position was restricted to be within the base of support boundaries marked by the heels and head of metatarsals, while the velocity and acceleration were to be 0. To avoid unreasonable solutions, the orientation of the trunk segment was also constrained; at all times, the trunk's angle was to be within $\pm60°$with respect to the vertical and its speed could not exceed $|200|°/s$ [27]. At t_f, the trunk was to be upright and motionless signifying a return to quiet stance [26]. Box constraints in (12) restricted joint motion to be within manufacturer-specified ranges for the Exo-H3; motor inputs had to stay within the nominal voltage. The nonlinear programming problem was solved using `fmincon` (MATLAB) with analytical gradients provided using ADiGator automatic differentiation software [25].

B. Simulation Experiment A

For experiment A, the FSR of the human-only was established with a variable dead time (DT). Following a perturbation, the central nervous system typically responds with a 75-120 ms delay [7], [26]. To mimic this in our simulations, we first determined the static torques required to hold the system's initial configuration static. We would then modify the control problem constraints such that for the first T ms, the control inputs could not deviate from the static values.

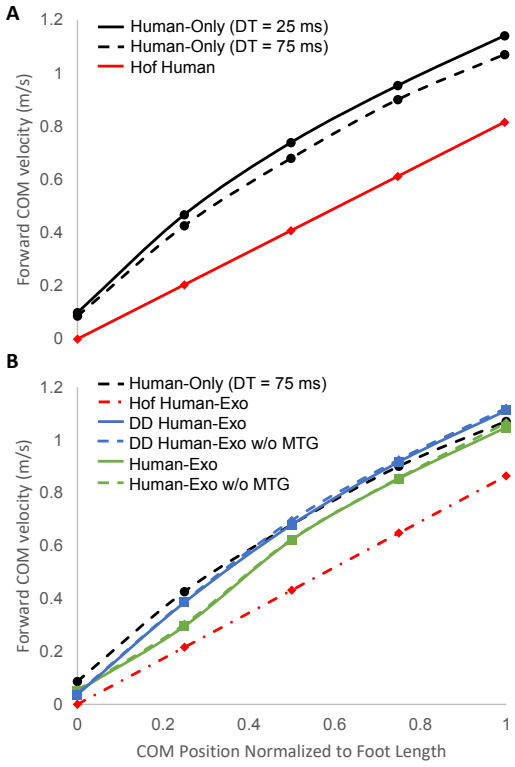

Fig. 2. The feasible stability region for the **A**) human-only and **B**) human-exo systems analyzed in experiment A. A reminder, for a given COM position normalized to foot length (0 = toe, 1 = heel), if the COM velocity is below the FSR boundary, then the biped can terminate this velocity such that quiet, upright stance can still be reached. If the velocity goes beyond this boundary, then the model must take a step (not analyzed herein) or fall. Note that "Hof Exo" refers to values returned by the Hof model with the lowered human-exo pendulum length; DD refers to direct drive.

The human model was then tested with a $T = 25$ and 75 ms dead time, with the latter being consistent with the delays implemented in existing biomechanics simulations [26]. With the human-only FSR established, we then estimated the FSR of the integrated human-exo model under a variety of conditions. The first set of simulations predicted how the device actuators alone, i.e. no active MTG torques, could balance the integrated system. This FSR was then compared to that generated when the end-user could generate active torques in synergy with the device. The second simulations then aimed to assess how the FSR in both cases presented in the first simulations would change when the actuator had low impedance similar to a direct-drive mechanism (DD). The low-impedance condition removed all gearing friction and reflected inertia from the equations, but still amplified the motor torque by N. Note that for all human-exo simulations, human and device dead time were kept at 75 ms and 25 ms respectively, where the latter was kept short to avoid large "anticipatory" torques at t_0.

C. Simulation Experiment B

Experiment B assessed the trade-off in motor torque generation in the device actuators with the FSR boundary.

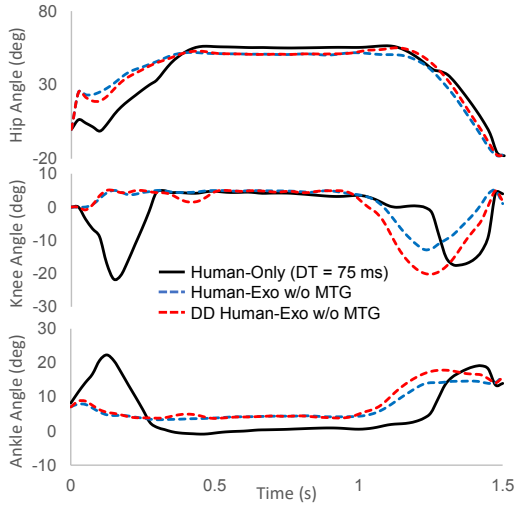

Fig. 3. Representative joint trajectories for the balance recovery strategies when the human-only (DT = 75 ms) and human-exo (without active MTG inputs) with and without direct-drive (DD) are initially located at the FSR boundary velocity at a normalized COM position 0.25 foot lengths behind the toes.

To do so, the cost function (8) was augmented such that the optimal control problem was now seeking

$$\arg\min_{\mathbf{X},\mathbf{U}} \{(1-\alpha)w_1(-\dot{\mathbf{r}}_{\mathrm{cm}}(t_0)\cdot\hat{\mathrm{i}}) + \alpha w_2 \sum_{i=1}^{6}\int_{t_0}^{t_f}(\tau_m)_i^2\, dt\} \tag{13}$$

where $(\tau_m)_i$ is the torque in motor i. This change effectively scalarizes the two objectives represented by the two terms in (13), which allows us to estimate the Pareto front of these objectives by evaluating the equation across the interval $\alpha \in [0,1]$. To handle differences in scaling between objectives, weights w_1 and w_2 were set to the inverse of their associated term evaluated at $\alpha = 0$ ($w_1 = 0.61^{-1}$s/m, $w_2 = 48732^{-1}$ N^{-2}m^{-2}). The optimal control problem was then solved at a normalized COM position for each value of α in $\{0, 0.1, ..., 1\}$.

IV. RESULTS AND DISCUSSION

A. Feasible Stability Region: Human-Only vs Human-Exo

For reference, the upper boundary of the system's FSR was also estimated using the linear inverted pendulum model by Hof et al. [14] (based on the ankle strategy [7]),

$$\max\{\dot{\mathbf{r}}_{\mathrm{cm}}(t_0)\cdot\hat{\mathrm{i}}\} = \sqrt{\frac{g}{\ell}}(r_{ub} - \mathbf{r}_{\mathrm{cm}}(t_0)\cdot\hat{\mathrm{i}}) \tag{14}$$

where g is acceleration due to gravity and r_{ub} is the distance from the ankle to toe. Pendulum length ℓ was set to 1.10 m for the human-only and 0.98 m for the human-exo model.

Fig. 2**A** displays the FSR boundary for the human-only model with a 25 and 75 ms dead time. Likewise, the predicted FSR from the Hof model is included. Evidently, the human-only model outperforms the Hof model in terminating higher initial velocities regardless of dead time. This is unsurprising given the improvements in upright balance recovery when humans are able to counter-rotate their body

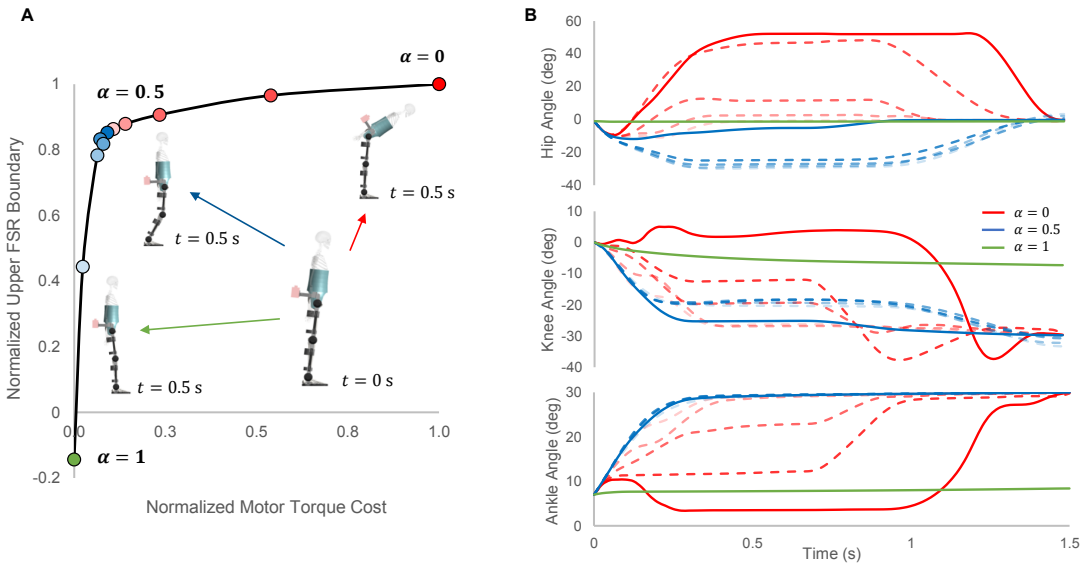

Fig. 4. **A**) The Pareto front of the evaluated squared torque cost against the maximal forward COM velocity that could be terminated, i.e.upper FSR boundary, and **B**) the change in balance recovery joint trajectories along the Pareto front. Both costs were normalized to their values at $\alpha = 0$. Sets of trajectories are colored to indicate what range of α was used to generate said result: red, α from 0 to 0.4; blue, α from 0.5 to 0.9; and green, $\alpha = 1$. Solid lines were used to identify trajectories at α = 0, 0.5, and 1 with intermediate steps between them shown through dotted lines.

segments [27], [12], [7], [14]. The increased dead time in the human-only model seemed to affect the FSR as well; the boundaries generated using two different DTs diverged from each other as the COM position was shifted towards and past the heels (Fig. 2). Fig. 2**B** displays the FSR for the balancing human-exo model. For comparison, the human-only results (dead time = 75 ms) are shown again. The human-exo system outperformed predictions by the Hof model highlighting how the device can execute feet-in-place balance recovery strategies well beyond the ankle strategy [7]. With that said, despite the exoskeleton lowering the system COM, the human-exo model generally had a lower FSR boundary with respect to the human-only.

To assess why the human-exo model had a smaller FSR, we can examine the balance recovery strategies used by the different models when the initial COM velocity was at its boundary value (Fig. 3). When the initial normalized COM position was 0.25 foot lengths behind the toe (toe = 0), the human-exo model could tolerate considerably lower COM velocities relative to the human-only (Fig. 2**B**). This observation was less apparent when the direct-drive (DD) mechanism was used in simulations. Regardless of DD, the human-exo model was not able to execute the initial burst of knee flexion and ankle dorsiflexion that the human-only used during the first 500 ms. Knee flexion has been previously shown to theoretically improve the FSR in human models [27]. Instead, the human-exo relied on rapid and early hip flexion, acting as more of a double-pendulum until the trunk had to be returned to upright. With DD, the human-exo was able to achieve greater knee and ankle motion towards the end of the simulation, likely due to the lowered joint-level impedance. These later bursts of motion return the system to upright equilibrium quicker and thus allow it to tolerate greater initial forward velocities. So, while the benefits of a low-impedance actuator are not evident in the early portion of balance recovery, later corrections for upright posture can improve. Furthermore, while the benefit of a lowered COM is well-described within the ankle strategy [14], it is not as clear for higher degree of freedom strategies and may depend more on the distribution of mass throughout the device.

Another notable observation was that the human-exo FSR appeared to exceed the human-only boundary at further posterior COM positions. Such improvements may be noticeable in actions like gait termination, where the COM is behind/over the front heel at contralateral toe-off [11]. Lastly, providing the simulated end-user with active MTG components had no clear effect on the human-exo FSR, regardless of whether they had to backdrive against high-density gearing. In these regards, low mobility users, e.g. paraplegics, could theoretically balance as well as a healthy baseline individual without need to contribute to the motion. On that note, we are limited in interpreting our results across all end-users. Issues experienced by those with mobility deficits, like variable muscle spasticity, reduced afferent/efferent conduction velocity, heightened spinal reflexes etc., were not considered and could impact how the exoskeleton is able to automate balance recovery [28]. With that said, the results still provide information with regards to how well electric actuators can substitute active muscle torques.

B. Trade-offs in Stability with Minimizing Motor Torques

Fig. 4 displays the results of the Pareto optimization that searched for the trade-offs in FSR size that come with

concurrent minimization of motor torques in the assistive device actuators. From this novel analysis, we could observe that substantial magnitudes of hip flexion requiring large motor torques are not necessary to achieve a good FSR. In fact, small increases in the motor torque cost when near 0 yield disproportionately larger improvements in the FSR size as seen from $\alpha = 1$ to $\alpha = 0.5$. By $\alpha = 0.5$, the FSR has already reached 85% of its maximal theoretical value. The final 15% improvement from $\alpha = 0.5$ to $\alpha = 0$ comes from a large increase in the required motor torques, less knee flexion and ankle dorsiflexion, as well as greater hip flexion. Information like this can be very important for design engineers. A control engineer may prefer a strategy like those indicated by the blue trajectories ($0.5 \leq \alpha \leq 0.9$) in Fig. 4**B** if they desire a longer lifetime for the device. Shifting the strategy towards the red trajectories ($\alpha \leq 0.4$) would allow the controller to withstand greater perturbations, but may reduce safety/comfort for the user. The actuator hardware may also be put at risk due to greater torque demand and power consumption. For example, increasing $\alpha = 0.1$ to $\alpha = 0.2$ increased the peak torque required by the hip actuator from 87.5 Nm to 118 Nm, while also increasing the peak power drawn by the motor from 54.4 W to 243 W.

V. CONCLUSIONS

In conclusion, we used dynamic simulations and optimal control to estimate how the FSR behaves for a typical robotic lower-limb exoskeleton when merged with the end-user, and how it is affected when avoiding large motor torques in the underlying control law. Our results suggest that lower-limb assistive devices are capable of balancing nearly as well as healthy young adults, though the high-impedance from the actuator and distribution of mass within the device appears to be a limiting factor. Additionally, observations from our Pareto optimization suggest that low-torque strategies can be used to provide the system with a large FSR whilst avoiding unecessary actuator outputs that could damage the hardware. While we examined fixed-support balance strategies herein, the formulation of our biped models with a floating base will allow us to examine research questions pertaining to the FSR with stepping strategies in the future. This research will be used in the design and implementation of safe and effective balance assistive controllers for the Technaid Exo-H3 [1].

REFERENCES

[1] K. A. Inkol and J. McPhee, "Assessing Control of Fixed-Support Balance Recovery in Wearable Lower-Limb Exoskeletons Using Multibody Dynamic Modelling," *8th IEEE RAS/EMBS International Conference for Biomedical Robotics and Biomechatronics*, 2020.

[2] V. Rajasekaran, J. Aranda, A. Casals, and J. L. Pons, "An Adaptive Control Strategy for Postural Stability Using a Wearable Robot," *Rob. Auton. Syst.*, vol. 73, pp. 16-23, 2015.

[3] T. Gurriet, S. Finet, G. Boeris, A. Duburcq, A. Hereid, O. Harib, M. Masselin, J. Grizzle, A. D. Ames, "Towards Restoring Locomotion for Paraplegics: Realizing Dynamically Stable Walking on Exoskeletons," *IEEE International Conference on Robotics and Automation*, 2018.

[4] R. M. Schemschat, D. Clever, K. Mombaur, "Optimization-Based Analysis of Push Recovery During Walking Motions to Support the Design of Lower-Limb Exoskeletons," *IEEE International Conference on Simulation, Modeling, and Programming for Autonomous Robots (SIMPAR)*, 2016.

[5] A. R. Emmens, E. H. F. van Asseldonk, M. Masciullo, M. Arquilla, I. Pisotta, "Improving the Standing Balance of Paraplegics through the Use of a Wearable Exoskeleton," *7th IEEE International Conference on Biomedical Robotics and Biomechatronics (Biorob)*, 2018.

[6] A. R. Emmens, E. H. F. van Asseldonk, H. van der Kooij, "Effects of a Powered Ankle-Foot Orthosis on Perturbed Standing Balance," *J. NeuroEng. Rehabil.*, vol. 15, pp. 50, 2018.

[7] L. M. Nashner, C. L. Shupert, F. B. Horak, F. O. Black, "Organization of Posture Controls: An Analysis of Sensory and Mechanical Constraints," *Progress in Brain Research*, vol. 80, pp. 411-418, 1989.

[8] J. F. Veneman, R. Kruidhof, E. E. Hekman, R. Ekkelenkamp, E. H. van Asseldonk, and H. van der Kooij, "Design and Evaluation of the LOPES Exoskeleton Robot for Interactive Gait Rehabilitation," *IEEE Trans Neural Syst Rehabil Eng.*, vol. 15, pp. 379-86, 2007.

[9] G. Marinou, M. Millard, N. Šarabon, and K. Mombaur,"Comparing the Risk of Low-Back Injury Using Model-Based Optimization: Improved Technique versus Exoskeleton Assistance," *Wearable Technologies*, vol. 2, 2021.

[10] Y.C. Pai and J. Patton, "Center of Mass Velocity-Position Predictions for Balance Control," *J. Biomech.*, vol. 30, pp. 347-354, 1997.

[11] F. Yang, F. Espy, and Y.C. Pai, "Feasible Stability Region in the Frontal Plane During Human Gait," *Ann. Biomed. Eng.*, vol. 37, pp.2606-2614, 2009.

[12] J. Pratt, J. Carff, S. Drakunov and A. Goswami, "Capture Point: A Step toward Humanoid Push Recovery," *6th IEEE-RAS International Conference on Humanoid Robots*, 2006.

[13] M. Millard, D. Wight, J. McPhee, E. Kubica, D. Wang, "Human Foot Placement and Balance in the Sagittal Plane," *J. Biomech. Eng.*, vol. 131, 2009.

[14] A. L. Hof, M. G. Gazendam, and W. E. Sinke, "The Condition for Dynamic Stability," *J. Biomech.*, vol.38, pp. 1-8, 2005.

[15] P. de Leva, "Adjustments to Zatsiorsky-Seluyanov's Segment Inertia Parameters," *J. Biomech.*, vol. 29, pp. 1223-30, 1996.

[16] K. A. Inkol, C. Brown, W. Mcnally, C. Jansen, and J. McPhee, "Muscle Torque Generators in Multibody Dynamic Simulations of Optimal Sports Performance," *Multibody Syst Dyn*, vol. 50, pp. 435–452, 2020.

[17] M. Millard, A. L. Emonds, M. Harant, and K. Mombaur, "A Reduced Muscle Model and Planar Musculoskeletal Model Fit for the Simulation of Whole-Body Movements," *J. Biomech*, vol. 24, pp.11-20, 2019.

[18] G. T. Yamaguchi, "Dynamic Modeling of Musculoskeletal Motion: A Vectorized Approach for Biomechanical Analysis in Three Dimensions," Springer, Boston, MA, 2005.

[19] D. E. Anderson, M. L. Madigan, and M. A. Nussbaum, "Maximum Voluntary Joint Torque as a Function of Joint Angle and Angular Velocity: Model Development and Application to the Lower Limb," *J. Biomech.*, vol. 40, pp. 3105–3113, 2007.

[20] R. Riener and T. Edrich, "Identification of Passive Elastic Joint Moments in the Lower Extremities," *J. Biomech.*, vol. 32, no. 5, pp. 539–544, 1999.

[21] J. Hauschild and G. R. Heppler, "Control of Harmonic Drive Motor Actuated Flexible Linkages," *Proceedings 2007 IEEE International Conference on Robotics and Automation*, 2007.

[22] P. Brown and J. McPhee, "A Continuous Velocity-Based Friction Model for Dynamics and Control With Physically Meaningful Parameters," *J. Comput. Nonlinear Dynam.*, vol. 11, 2006.

[23] Maxon EC-max 40 Motor Catalog Page, https://www.maxongroup-.com/medias/sys_master/root/8882556567582/EN-21-253.pdf, 2021.

[24] HarmonicDrive Reducer Catalog, https://www.harmonicdrive.net/_hd/content/documents1/FR_Component.pdf.

[25] M. J. Weinstein and A. V. Rao, "Algorithm 984: ADiGator, a Toolbox for the Algorithmic Differentiation of Mathematical Functions in MATLAB Using Source Transformation via Operator Overloading," *ACM Transactions on Mathematical Software (TOMS)*, vol. 44, 2017.

[26] C. S. Versteeg, L. H. Ting, and J. L. Allen, "Hip and Ankle Responses for Reactive Balance Emerge from Varying Priorities to Reduce Effort and Kinematic Excursion: A Simulation Study," *J. Biomech.*, vol. 49, pp. 3230-3237, 2016.

[27] K.Iqbal and Y. C. Pai, "Predicted Region of Stability for Balance Recovery: Motion at the Knee Joint can Improve Termination of Forward Movement," *J. Biomech.*, vol. 30, pp. 1619-27, 2000.

[28] G. Durandau and M. Goldfarb, "Supplemental Stimulation Improves Swing Phase Kinematics During Exoskeleton Assisted Gait of SCI Subjects With Severe Muscle Spasticity ," *Front. Neurosci-Switz.*, vol. 12, 2018.